Synthesis and Delamination of Layered Manganese Oxide Nanobelts

Zhaoping Liu, Renzhi Ma, Yasuo Ebina, Kazunori Takada, and Takayoshi Sasaki*

Nanoscale Materials Center, National Institute for Materials Science (NIMS), Namiki 1-1, Tsukuba, Ibaraki 305-0044, Japan

Received July 19, 2007. Revised Manuscript Received September 25, 2007

This paper describes systematic studies on the synthesis and delamination of manganese oxide nanobelts with the birnessite-type layered structure. K-birnessite nanobelts of $K_{0.33}MnO_2 \cdot 0.5H_2O$, which typically had a length of several tens of micrometers, a width of hundreds of nanometers, and a thickness of ~15 nm, were synthesized by hydrothermally treating a $KMnO_4$–$MnCl_2$ mixture in a highly concentrated KOH aqueous solution. The nanobelt growth was found to be controlled by the KOH concentration and the molar ratio of Mn^{2+}/MnO_4^- in the starting reaction mixture. The K-birnessite nanobelts were converted to H-birnessite, $H_{0.08}MnO_2 \cdot 0.7H_2O$, by treatment with a $(NH_4)_2S_2O_8$ aqueous solution, retaining their high crystallinity and beltlike morphology. Swelling and delamination behaviors of the H-birnessite nanobelts in aqueous solutions of quaternary ammonium hydroxides were studied in detail. In tetrabutylammonium hydroxide (TBAOH) solutions, the H-birnessite showed a limited swelling and delamination behavior, whereas the compound underwent osmotic swelling in tetramethylammonium hydroxide (TMAOH) solutions. Water-washing the TMA^+-treated samples greatly enhanced the degree of swelling, while maintaining the three-dimensional crystalline order. Upon further contact with a TBAOH solution, the highly swollen phase was dominantly delaminated into unilamellar nanosheets. The nanosheets thus obtained inherited the morphology of the parent nanobelts in their long-axis direction and had lateral sizes of micrometer order. The colloidal suspension of nanosheets showed an optical absorption band around 380 nm, which was drastically changed from the rather constant and featureless absorption of UV to visible light for the birnessite before delamination.

Introduction

Birnessite is a member of the layered manganese oxide compounds, which consist of coplanar layers of edge-shared MnO_6 octahedra accommodating exchangeable cations and water molecules in the interlayer space. The heterovalent Mn cations (i.e., Mn^{3+} and Mn^{4+}) result in a net negative charge for the MnO_2 basal layers, which is balanced by the interlayer cations. The chemical composition of birnessite can be expressed by the general formula of $A_xMnO_2 \cdot yH_2O$, where A is H^+ or a metal cation such as K^+, Na^+, and Ca^{2+}.[1] Birnessite materials have received increasing attention in recent years, owing to their wide range of applications as ion-exchangers,[2] selective adsorbents,[3] catalysts,[4] electrode materials,[5] and so on. Natural birnessite minerals are usually of extremely fine crystallites and often accompanied by a considerable amount of impurities, which hinder not only fundamental studies on physicochemical properties but also some advanced technological applications. Therefore, the synthesis of high-quality birnessite is of both fundamental and practical importance.

Birnessite is synthesized easily under laboratory conditions through the following four routes: oxidation of Mn^{2+},[6] reduction of MnO_4^-,[7] redox reactions between Mn^{2+} and MnO_4^-,[8] and direct conversion of manganese oxides (e.g., γ-MnOOH, Mn_2O_3, MnO_2, etc.).[9] To understand well

---

* Corresponding author. E-mail: sasaki.takayoshi@nims.go.jp.

(1) Post, J. E.; Veblen, D. R. *Am. Mineral.* **1990**, *75*, 477 and references therein.

(2) (a) Straczek, J. R.; Horen, A.; Warshaw, C. M. *Am. Mineral.* **1960**, *45*, 1174. (b) Golden, D. C.; Dixon, J. B.; Chen, C. C. *Clays Clay Miner.* **1986**, *34*, 511. (c) Burns, R. G.; Burns, V. M.; Stockman, H. W. *Am. Mineral.* **1983**, *68*, 972.

(3) (a) Tu, S. H.; Racz, G. J.; Goh, T. B. *Clays Clay Miner.* **1994**, *42*, 321. (b) Paterson, E.; Swaffield, R.; Clark, L. *Clay Miner.* **1994**, *29*, 215. (c) Le Goff, P.; Baffier, N.; Bach, S.; Pereira-Ramos, J. P. *Mater. Res. Bull.* **1996**, *31*, 63.

(4) (a) Nitta, M. *Appl. Catal.* **1984**, *9*, 151. (b) Jiang, S. P.; Ashton, W. R.; Tseung, A. C. C. *J. Catal.* **1991**, *131*, 88. (c) Shen, Y.-F.; Zerger, R. P.; Suib, S. L.; McCurdy, L.; Potter, D. I.; O'Young, C.-L. *J. Chem. Soc., Chem. Commun.* **1992**, 1213. (d) Wong, S. T.; Cheng, S. *Inorg. Chem.* **1992**, *31*, 1165. (e) Shen, Y. F.; Zerger, R. P.; DeGuzman, R. N.; Suib, S. L.; McCurdy, L.; Potter, D. I.; O'Young, C.-L. *Science* **1993**, *260*, 511. (f) Shen, Y.-F.; Suib, S. L.; O'Young, C.-L. *J. Catal.* **1996**, *161*, 115–122.

(5) (a) Bach, S.; Henry, M.; Baffier, N.; Livage, J. *J. Solid State Chem.* **1990**, *88*, 325. (b) Pereira-Ramos, J. P.; Baddour, R.; Bach, S.; Baffier, N. *Solid State Ionics* **1992**, *53–56*, 701. (c) Bach, S.; Pereira-Ramos, J. P.; Baffier, N. *Electrochim. Acta* **1993**, *38*, 1695. (d) Bach, S.; Pereira-Ramos, J. P.; Baffier, N. *J. Solid State Chem.* **1995**, *120*, 70. (e) Yang, X.; Makita, Y.; Liu, Z.-H.; Ooi, K. *Chem. Mater.* **2003**, *15*, 1228.

(6) (a) Feitknecht, W.; Marti, W. *Helv. Chim. Acta* **1945**, *28*, 129. (b) Wadsley, A. D. *J. Am. Chem. Soc.* **1950**, *72*, 1781. (c) Giovanoli, R.; Stahli, E.; Feitknecht, W. *Helv. Chim. Acta* **1970**, *53*, 209. (d) Golden, D. C.; Chen, C. C.; Dixon, J. B. *Science* **1986**, *231*, 717. (e) Luo, J.; Zhang, Q.; Suib, S. L. *Inorg. Chem.* **2000**, *39*, 741. (f) Liu, Z.-H.; Ooi, K.; Kanoh, H.; Tang, W.; Yang, X.; Tomida, T. *Chem. Mater.* **2001**, *13*, 473. (g) Cai, J.; Suib, S. L. *Inorg. Chem. Commun.* **2001**, *4*, 493. (h) Cai, J.; Liu, J.; Suib, S. L. *Chem. Mater.* **2002**, *14*, 2071.

(7) (a) McMurdie, H. F. *Trans. Electrochem. Soc.* **1944**, *86*, 313. (b) Leroux, F.; Guyomard, D.; Piffard, Y. *Solid State Ionics* **1995**, *80*, 299. (c) Ching, S.; Landrigan, J. A.; Jorgensen, M. L.; Duan, N.; Suib, S. L.; O'Young, C.-L. *Chem. Mater.* **1995**, *7*, 1604. (d) Chen, R.; Zavalij, P.; Whittingham, M. S. *Chem. Mater.* **1996**, *8*, 1275. (e) Ching, S.; Petrovay, D. J.; Jorgensen, M. L.; Suib, S. L. *Inorg. Chem.* **1997**, *36*, 883. (f) Ma, Y.; Luo, J.; Suib, S. L. *Chem. Mater.* **1999**, *11*, 1972. (g) Gao, Q.; Giraldo, O.; Tong, W.; Suib, S. L. *Chem. Mater.* **2001**, *13*, 778.

10.1021/cm7019203 CCC: $37.00

structural and crystal–chemical features of birnessite, and especially to further disintegrate the birnessite into well-defined single layers, the synthesis of large birnessite crystals is highly desirable. However, it is difficult to grow large or well-formed birnessite crystals except for those in a KNO_3 flux system reported recently.[9e]

Since the physical properties of manganese oxide crystals depend strongly on the morphology and size of the crystals,[5] special attention has also been paid in recent years to the shape-controlled synthesis of birnessite into one-dimensional nanoarchitectures.[8d,9f] Compared with hollandite manganese oxides with tunnel structure,[10] there are far fewer reports on the synthesis of layered birnessite with one-dimensional morphology. In fact, to date, there have been only two reports on the preparation of such one-dimensional nanomaterials through hydrothermal treatment of Mn precursors (Mn_2O_3 or a mixture of MnO_4^- and Mn^{2+}) in highly concentrated alkaline solutions.[8d,9f] The products in both reports were nanobelts with lengths of several tens of micrometers or more and lateral sizes of several tens of nanometers. These nanobelts showed an improved electric conductivity and electrochemical performance, as expected from the reduced dimensionality and size. However, owing to their small lateral sizes, these nanobelts had a disadvantage in some applications including the further preparation of large MnO_2 single layers. In addition, despite the successful synthesis of birnessite nanobelts, the anisotropic growth of the nanobelts is not well understood. Therefore, it is essential to optimize the synthetic parameters or to establish a new and feasible process for synthesizing nanobelts with a larger lateral size based on an understanding of the mechanism of the formation of the nanobelts.

Recently, the delamination of layered birnessite into its elementary layers has attracted significant interest because the resulting MnO_2 nanosheets exhibited distinctive catalytic, optical, electric, and magnetic properties in comparison with the parent material.[11] To date, three groups have reported on the swelling and delamination behaviors of protonic birnessite (i.e., H-birnessite) upon reactions with quaternary ammonium hydroxides, $(C_nH_{2n+1})_4NOH$ ($n = 1, 2, 3, 4$).[7g,11a–c] Ooi and co-workers studied the intercalation of tetramethylammonium (TMA), tetraethylammonium (TEA), tetrapropylammonium (TPA), and tetrabutylammonium (TBA) ions into H-birnessite of $H_{0.28}Na_{0.02}MnO_2 \cdot 0.8H_2O$ and found that a marked short-range swelling was induced by the TMA^+ intercalation while interlayer expansions barely occurred in the systems of larger ions.[11a] Furthermore, they succeeded in delaminating birnessite into MnO_2 single sheets by water-washing the TMA^+-intercalated phase. In their follow-up, similar results were obtained for $H_{0.22}MnO_2 \cdot 0.62H_2O$, derived from flux-grown K-birnessite crystals.[11c]

Suib's group also investigated intercalation reactions of H-birnessite with various quaternary ammonium ions and prepared nanometer-sized manganese oxides from the intercalating precursors.[7g] Recently, our group reported that the action of aqueous TBA ions on $H_{0.13}MnO_2 \cdot 0.7H_2O$ induced intercalation, osmotic swelling, and delamination into single sheets, depending on the TBA concentration.[11b] By comparison of these results, H-birnessite samples having different amounts of exchangeable protons may show different swelling and delamination behaviors upon contact with aqueous quaternary ammonium ions. To verify this presumption and also to produce high-quality MnO_2 single sheets at a high yield, a more detailed understanding of the swelling and delamination of various H-birnessite samples is needed.

In the present work, we carried out systematic studies on the synthesis and delamination of birnessite nanobelts. High-quality nanobelts of K-birnessite were hydrothermally synthesized in a $KMnO_4$–$MnCl_2$–KOH system with a molar Mn^{2+}/MnO_4^- ratio of 2. Detailed studies were carried out on the swelling and delamination behaviors of the protonated birnessite nanobelts in TMAOH and TBAOH solutions. A rational two-step delamination method was then established for the synthesis of MnO_2 single layers. Obtained birnessites and MnO_2 nanosheets were characterized in terms of chemical composition, structure, morphology, size, and optical absorption property.

Experimental Section

Chemicals. All chemicals used were of analytical grade and were purchased from Wako Chemical Reagents Company (Japan). Milli-Q filtered water was used throughout the experiments.

Synthesis of K-Birnessite Nanobelts. K-birnessite nanobelts were synthesized by hydrothermally treating a $KMnO_4$–$MnCl_2$–KOH mixture with a molar Mn^{2+}/MnO_4^- ratio of 2. In a typical procedure, 10 mmol of $KMnO_4$ was first dissolved into 280 cm^3 of water, and then 6 mol of solid KOH was added under vigorous stirring to form a hot, dark green solution. Then, 20 cm^3 of 1 M $MnCl_2$ aqueous solution was quickly introduced into this hot solution, after which the mixture was allowed to cool with continued stirring for 2 h. The resulting black slurry, having a volume of $\sim$450 cm^3, was then transferred into a Teflon-lined stainless steel autoclave. The autoclave was sealed and put in an electric oven at

---

(8) (a) Shen, Y.-F.; Suib, S. L.; O'Young, C.-L. *J. Am. Chem. Soc.* **1994**, *116*, 11020. (b) Luo, J.; Suib, S. L. *J. Phys. Chem. B* **1997**, *101*, 10403. (c) Luo, J.; Huang, A.; Park, S. H.; Suib, S. L.; O'Young, C.-L. *Chem. Mater.* **1998**, *10*, 1561. (d) Zhang, H. T.; Chen, X. H.; Zhang, J. H.; Wang, G. Y.; Zhang, S. Y.; Long, Y. Z.; Chen, Z. J.; Wang, N. L. *J. Cryst. Growth* **2005**, *280*, 292.

(9) (a) Hirano, S.; Narita, R.; Naka, S. *Mater. Res. Bull.* **1984**, *19*, 1229. (b) Morales, J.; Navas, J. J.; Tirado, J. L. *Solid State Ionics* **1990**, *44*, 125. (c) Feng, Q.; Kanoh, H.; Miyai, Y.; Ooi, K. *Chem. Mater.* **1995**, *7*, 1226. (d) Feng, Q.; Yamasaki, N.; Yanagisawa, K.; Ooi, K. *J. Mater. Sci., Lett.* **1996**, *15*, 963. (e) Yang, X.; Tang, W.; Feng, Q.; Ooi, K. *Cryst. Growth Des.* **2003**, *3*, 409. (f) Ma, R.; Bando, Y.; Zhang, L.; Sasaki, T. *Adv. Mater.* **2004**, *16*, 918.

(10) For example: (a) Xia, G.-G.; Tong, W.; Tolentino, E. N.; Duan, N.-G.; Brock, S. L.; Wang, J.-Y.; Suib, S. L.; Ressler, T. *Chem. Mater.* **2001**, *13*, 1585. (b) Wang, X.; Li, Y. *J. Am. Chem. Soc.* **2002**, *124*, 2880. (c) Wang, X.; Li, Y. *Chem. Commun.* **2002**, 764. (d) Wang, X.; Li, Y. *Chem. Eur. J.* **2003**, *9*, 300. (e) Shen, X.; Ding, Y.; Liu, J.; Laubernds, K.; Zerger, R. P.; Polverejan, M.; Son, Y.-C.; Aindow, M.; Suib, S. L. *Chem. Mater.* **2004**, *16*, 5327. (f) Villegas, J. C.; Garces, L. J.; Gomez, S.; Durand, J. P.; Suib, S. L. *Chem. Mater.* **2005**, *17*, 1910. (g) Wu, M.-S.; Chiang, P.-C. J.; Lee, J.-T.; Lin, J.-C. *J. Phys. Chem. B* **2005**, *109*, 23279.

(11) (a) Liu, Z.-H.; Ooi, K.; Kanoh, H.; Tang, W.-P.; Tomida, T. *Langmuir* **2000**, *16*, 4154. (b) Omomo, Y.; Sasaki, T.; Wang, L. Z.; Watanabe, M. *J. Am. Chem. Soc.* **2003**, *125*, 3568. (c) Yang, X.; Makita, Y.; Liu, Z.-H.; Sakane, K.; Ooi, K. *Chem. Mater.* **2004**, *16*, 5581. (d) Sakai, N.; Ebina, Y.; Takada, K.; Sasaki, T. *J. Phys. Chem. B* **2005**, *109*, 9651. (e) Cui, Y.; Liu, Z.-H.; Wang, M.; Ooi, K. *Chem. Lett.* **2006**, *35*, 740. (f) Suzuki, S.; Takahashi, S.; Sato, K.; Miyayama, M. *Key Eng. Mater.* **2006**, *320*, 223. (g) Sasaki, T. *J. Ceram. Soc. Jpn.* **2007**, *115*, 9.

175 °C for 2 days and then allowed to cool naturally to room temperature. The hydrothermal treatment resulted in a dark gray solid. The product was collected from the concentrated alkaline solution, rinsed thoroughly with water to remove KOH residue, and then air-dried.

Protonation. Conversion of K-birnessite to H-birnessite was carried out by doubly treating with a $(NH_4)_2S_2O_8$ aqueous solution. Typically, 2 g of as-prepared K-birnessite was dispersed into 500 cm^3 of a 0.5 M $(NH_4)_2S_2O_8$ aqueous solution. The mixture was stirred at 60 °C for 3 h. The solid was filtered and washed with water and then treated again with the $(NH_4)_2S_2O_8$ aqueous solution. The final sample was recovered using the same procedure as described for the pristine material.

Exfoliation. A weighed amount (0.1 g) of as-prepared H-birnessite was immersed in 25 cm^3 of aqueous TMAOH solution. The resulting slurry was shaken at 120 rpm for 2 days. The dose of TMAOH applied with respect to the amount of exchangeable protons in the H-birnessite (formulated as $H_{0.08}MnO_2 \cdot 0.7H_2O$), namely the molar ratio of TMA^+/H^+, was varied between 1 and 1000 by adjusting the concentration of TMAOH. The equilibrated mixture of H-birnessite and TMAOH solution, with a TMA^+/H^+ ratio of >30, was centrifuged and water-washed repeatedly until the supernatant solution became neutral. Then, the centrifuged pastelike sediment was dispersed in a TBAOH solution of various concentrations to make a final volume of 25 cm^3. The mixture was shaken moderately (80 rpm) for 2 days to achieve delamination.

Characterization. K and Mn contents were determined by inductively coupled plasma (ICP) atomic emission spectrophotometry (Seiko SPS1700HVR) after dissolving a weighed amount of sample into a mixed solution of HCl and H_2O_2. The mean valence of Mn, Z_{Mn}, was determined by standard titration using sodium oxalate.[12] The water content was estimated by thermogravimetry.

Thermogravimetric–differential thermal analysis (TG-DTA) measurements were carried out using a Rigaku TGA-8120 instrument in the temperature range of 25–1100 °C at a heating rate of 5 °C min^{-1}. X-ray diffraction (XRD) data were collected by a Rigaku Rint-2000S diffractometer equipped with graphite-monochromatized Cu Kα radiation ($\lambda = 0.154\,05$ nm). For the wet samples, the relative humidity in the sample chamber was regulated at 95% to suppress undesirable drying. Scanning electron microscopy (SEM) images were taken with a JEOL JSM-6700F microscope. Transmission electron microscopy (TEM) images and selected-area electron diffraction (SAED) patterns were obtained using a JEOL JEM-3000F microscope at an accelerating voltage of 300 kV. UV–vis absorption spectra were recorded with a Hitachi U-4100 spectrophotometer. A Seiko SPA 400 atomic force microscopy (AFM) system was used to examine the topography of nanosheets deposited onto a Si wafer substrate precoated with polyethylenimine (PEI). AFM images were acquired in tapping mode using a Si tip cantilever with a force constant of 20 N m^{-1}.

Results and Discussion

Synthesis of K-Birnessite Nanobelts. Figure 1 shows an XRD pattern of the dark gray product obtained in the hydrothermal $KMnO_4$–$MnCl_2$–KOH system. All the diffraction peaks could be readily indexed as a monoclinic structure [space group: *C*2/*m* (12)] with the refined unit-cell parameters of $a = 0.5160$ (2) nm, $b = 0.2841$ (1) nm, $c = 0.7165$ (1) nm, and $\beta = 100.25(1)°$, which are very close to the reported data for K-birnessite.[1] The diffraction peaks were sharp and symmetric, indicating that the as-prepared birnessite was well crystallized. There were still a few weak impurity peaks in a 2θ range of 15°–35°, which may be identified as a hausmannite phase (i.e., Mn_3O_4). In view of the rather faint features, the amount was almost negligible. The presence of hausmannite may be due to the fact that a small amount of Mn(II) (in the form of $Mn(OH)_2$) was oxidized to hausmannite by air at the initial stage of synthesis, as explained in previous reports.[1]

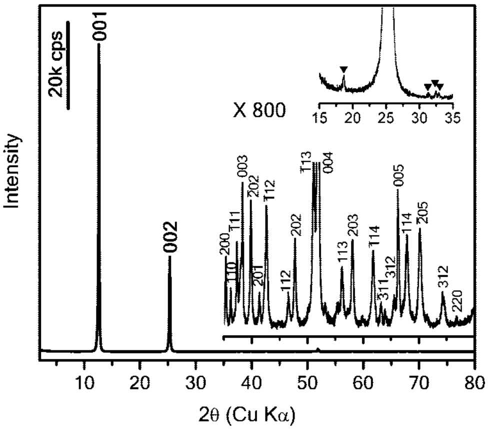

Figure 1. XRD pattern of the as-prepared K-birnessite sample. (insets) Enlarged view of the pattern in the 2θ range of 15°–35° and a higher angular region. The small peaks designated by triangles in the upper inset were assigned to the hausmannite phase.

According to the results of elemental analysis and thermogravimetric measurement (Supporting Information, Figure S1), the obtained birnessite could be formulated as $K_{0.33}MnO_2 \cdot 0.5H_2O$ (Anal. Calcd: K, 11.9%; Mn, 50.7%; H_2O, 7.8%. Found: K, 12.0%; Mn, 50.7%; H_2O, 7.8%). This formula gives a layer negative charge of 0.33 per Mn atom. By the standard titration with sodium oxalate, the mean valence of Mn, Z_{Mn}, was estimated to be 3.68, which is compatible with that of the empirical formula based on chemical analysis.

Shown in the inset of Figure 2a is the as-prepared dark gray product dispersed in water. The sample glittered in light, indicating the presence of anisotropically shaped crystallites with a considerable size. In practice, SEM images (Figure 2) revealed that the sample was dominated by long nanobelts. The nanobelts were very thin and had lengths of several tens of micrometers and widths mainly in the range of 300–1000 nm, which is much larger than the nanobelts of several tens of nanometers in width in the previous studies.[8d,9f] The thickness of different nanobelts was rather uniform, which was estimated by cross-sectional SEM imaging to be ~15 nm. Moreover, most of the unbroken nanobelts were found to have angular tips (indicated by arrows) with a specific angle approximately equal to 120°. This morphology is related to particular crystal planes serving as growth front, as will be described later. Besides the dominant nanobelts, sporadic nanoparticles (tens of nanometers in size) adhered on the surface of nanobelts were sometimes found. These particles should be identified as the hausmannite phase.

---

(12) Japan Industrial Standard N8233, Methods for Determination of Active Oxygen in Manganese Ores; Japanese Industrial Standards Committee, **1969**.

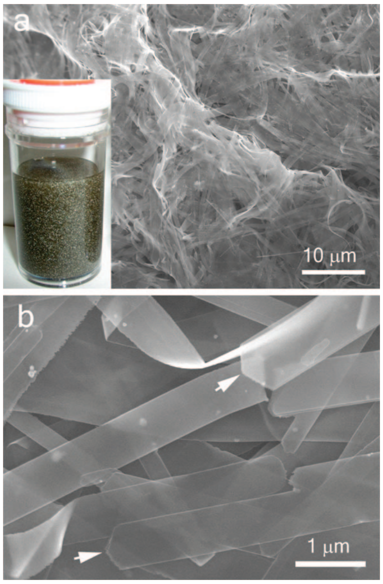

Figure 2. Low- and high-magnification SEM images of the K-birnessite sample. Panel a (inset): Bottle of K-birnessite sample dispersed in water.

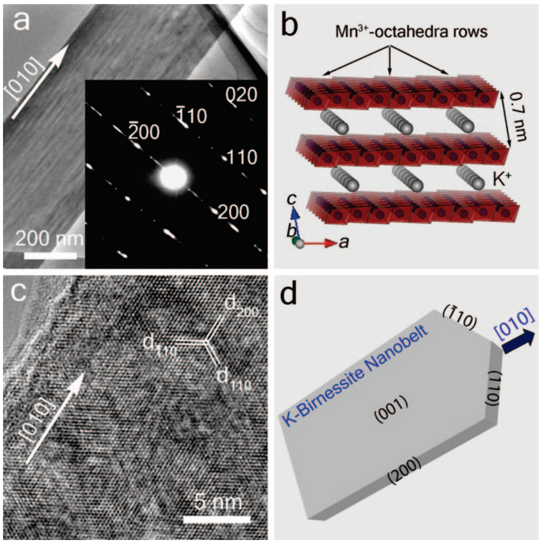

Figure 3. (a) TEM image of a K-birnessite nanobelt lying on a Cu grid. Inset is the corresponding SAED pattern obtained with the electron beam perpendicular to the wide surface of the nanobelt. (b) Schematic illustration for an idealized layer structure of monoclinic K-birnessite. Water molecules are not shown for clarity. (c) High-resolution TEM image recorded near the edge of the nanobelts. (d) Crystallographic facets and the orientation of K-birnessite nanobelt.

Figure 3a shows a TEM image of K-birnessite nanobelt. The corresponding SAED pattern (inset of Figure 3a) contains a set of strong *hk*0 diffraction spots arranged according to a pseudohexagonal symmetry, which are attributable to in-plane (i.e., *ab*-plane) reflections of birnessite. As a noteworthy additional feature, there were weak superstructure reflections corresponding to a supercell with parameters $A = 3a = 1.548$ nm, $B = b = 0.284$ nm, and $\gamma = 90°$, which are similar to those of previous reports.[1] The extra spots have been understood to be due to a superstructure, in which each row of consecutive Mn^{3+} octahedra in parallel to the *b*-axis was separated along the *a*-axis by two rows of successive Mn^{4+} octahedra.[13] This distribution mode for Mn^{3+} and Mn^{4+} in the birnessite structure has been evidenced by EXAFS analysis.[14] The ordered arrangement of Mn^{3+} octahedra should result in the distribution of interlayer K^+ either above or below Mn^{3+} octahedra to minimize the electrostatic repulsion, as schematically depicted in Figure 3b. Such an idealized structure agrees well with the chemical composition for the present K-birnessite sample. However, these superlattice spots extended into diffuse streaks parallel to the *a*-axis, indicating that the triplet periodicity of the Mn^{3+}/K^+ rows was involved by some disorder.

The high-resolution TEM image (Figure 3c) recorded near the edge of the nanobelts showed three sets of distinct spacings of ~0.25 nm, which correspond to the (200) lattice plane and two equivalent planes of (110) and ($\bar{1}10$). These data clearly indicate that each nanobelt was a single crystal, growing along the [010] direction, namely the *b*-axis, of monoclinic birnessite and that the crystallite was enclosed by ±(001) top and bottom surfaces, ±(200), ±(110), and ±($\bar{1}10$) side surfaces, as schematically illustrated in Figure 3d. The calculated apex angle (120°) between the growth front planes, (110) and ($\bar{1}10$), or ($\bar{1}\bar{1}0$) and ($1\bar{1}0$), is consistent with the observed one at the nanobelt ends. These equivalent planes serving as growth fronts of the birnessite crystal may be due to their relatively higher surface energy, which led to a symmetrical and faster growth along the *b*-axis.

The current synthesis yielded a special beltlike morphology for K-birnessite, which was distinctly different from the flakelike, fiberlike, and prismlike crystallites reported earlier.[1,6–9] It is important to understand the mechanism of the formation of the nanobelts and the effects of key synthetic parameters on the nanobelt growth. The former may be clarified by examining the sample prior to the hydrothermal treatment. XRD and SEM measurements (Figure S2) revealed that the nonhydrothermal sample was mainly composed of small nanoplates (50–500 nm in lateral size and ~15 nm in thickness) of crystalline K-birnessite. These results strongly suggest that the nanobelts grow through a dissolution–recrystallization mechanism, which has been proposed to explain the growth of various one-dimensional nanostructures.[15] The smaller platelets, due to a higher free energy, are gradually redissolved into the hydrothermal solution, finally leading to a supersaturated solution of "birnessite". The solution then precipitates out onto the surfaces of larger platelets. The recrystallization would preferentially occur on the surfaces of higher surface free energies, namely ±(110) and ±($\bar{1}10$) crystallographic faces. The continuous and fast growth on these surfaces of the large platelets results in beltlike structures along the [010] direction. The growth on the surfaces of relatively lower surface

---

[13] (a) Drits, V. A.; Silvester, E.; Gorshkov, A. I.; Manceau, A. *Am. Mineral.* **1997**, *82*, 946. (b) Lanson, B.; Drits, V. A.; Silvester, W.; Manceau, A. *Am. Mineral.* **2000**, *85*, 826.

[14] Ressler, T.; Brock, S. L.; Wong, J.; Suib, S. L. *J. Phys. Chem. B* **1999**, *103*, 6407.

[15] For example: (a) Yu, H.; Buhro, W. E. *Adv. Mater.* **2003**, *15*, 416. (b) Kudo, M.; Ohkawa, H.; Sugimoto, W.; Kumada, N.; Liu, Z.; Terasaki, O.; Sugahara, Y. *Inorg. Chem.* **2003**, *42*, 4479. (c) Sun, Y.; Mayers, B.; Herricks, T.; Xia, Y. *Nano Lett.* **2003**, *3*, 955. (d) Xi, G.; Xiong, K.; Zhao, Q.; Zhang, R.; Zhang, H.; Qian, Y. *Cryst. Growth Des.* **2006**, *6*, 577.

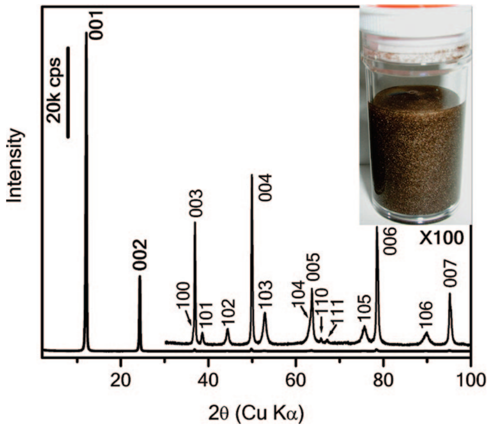

Figure 4. XRD pattern of H-birnessite sample obtained by double treatments of the K-birnessite with a $(NH_4)_2S_2O_8$ solution. (inset) Bottle of H-birnessite sample dispersed in water.

free energy, ±(001) surfaces, almost stopped, as evidenced by a negligible change in thickness during the hydrothermal treatment.

Our experiments revealed that the KOH concentration was a key factor influencing the nanobelt growth. In a typical experiment, the KOH solution had a concentration of as high as 13.3 M. In such a concentrated KOH solution, K-birnessite had a high solubility under the hydrothermal conditions, resulting in fast growth of the crystals. When KOH solutions of a lower concentration ($\leq$9 M) were used, the products were dominated by small platelets, as demonstrated by SEM images (Figure S3), indicating that a relatively low concentration of KOH was unfavorable for crystal growth due to the limited solubility of K-birnessite.

Moreover, the relative dose of $MnCl_2$ and $KMnO_4$ was found to be another crucial synthetic parameter that influenced the size and purity of the product (Figure S4). In the typical synthesis, the Mn^{2+}/MnO_4^- ratio was 2, at which the product was dominated by long nanobelts of K-birnessite. This means that 2 equiv of Mn^{2+} could react exactly with 1 equiv of MnO_4^-. When $Mn^{2+}/MnO_4^- > 2$, the products were contaminated by hausmannite particles, the amount of which increased as the Mn^{2+}/MnO_4^- ratio increased. The hausmannite impurity formed due to the excess of Mn^{2+}. On the other hand, when $Mn^{2+}/MnO_4^- < 2$, no hausmannite formed; however, the nanobelts became shorter. As the Mn^{2+}/MnO_4^- ratio decreased to 1.5, the product was composed of small platelets of micrometer size. The passivation effect of MnO_4^- could be suppressed to some extent in synthesis at elevated temperature. As recently reported by Zhang et al.,[8d] a hydrothermal temperature as high as 265 °C was required to prepare nanobelts at $Mn^{2+}/MnO_4^- = 1.5$.

Protonation of Birnessite. The protonation of the K-birnessite nanobelts was conducted by treatment with a $(NH_4)_2S_2O_8$ aqueous solution at 60 °C following a method reported by Ooi's group.[9e,11c] The extraction rate of K^+ reached 99.9% after double treatments (3 h for each treatment). The obtained H-birnessite sample showed a brown color (inset of Figure 4), which was distinct from the dark gray color of the pristine K-birnessite. This color change is associated with the increased Z_{Mn} of 3.92 as determined by titration. On the basis of this value as well as the results of elemental analysis and thermogravimetric measurement (Figure S5), the chemical composition of the H-birnessite sample was determined as $H_{0.08}MnO_2 \cdot 0.7H_2O$ (Anal. Calcd: Mn, 54.7%; ignition loss, 24.1%. Found: Mn, 54.6%; ignition loss, 24.1%). The proton content was deduced by taking into account the total charge neutrality.

Figure 4 shows XRD data of the resultant H-birnessite. All the diffraction peaks could be indexed on the basis of a primitive hexagonal unit cell with refined lattice parameters of $a = 0.2843(1)$ nm and $c = 0.7311(1)$ nm, which are consistent with those of H-birnessite in the literature.[13] The sharp reflections indicated well-retained high crystallinity. The structural transformation of monoclinic K-birnessite to hexagonal H-birnessite may be ascribed to the noticeably decreased amount of Mn^{3+}, which should release the steric strain arising from Jahn–Teller distortion. The apparent morphology of the crystals was well retained after the protonation.

The above observations confirm that the $(NH_4)_2S_2O_8$ solution was very effective for extracting K^+ ions from K-birnessite without an appreciable change in morphology and crystallinity. Protonation of birnessite in a normal acid solution such as HCl undergoes two concurrent processes: exchange of interlayer K^+ ions by protons and oxidative deintercalation of K^+ ions through disproportionation of Mn^{3+} in the layer into Mn^{4+} and Mn^{2+}.[13] The Mn^{2+} produced by the disproportionation transfers into the solution and thus leaves a cavity in the layer. This reaction degrades the sample quality and crystallinity. The $(NH_4)_2S_2O_8$ solution, on the other hand, behaves as a weak acid with a strong oxidizing power. No Mn^{2+} ions were detected in the reaction solution by EDTA titration, indicating that K^+ ions were deintercalated not by disproportionation of Mn^{3+} into Mn^{4+} and Mn^{2+}, but by direct oxidation of Mn^{3+} to Mn^{4+}. In addition to this process, moderate acid exchange proceeded via the weak acidity of the solution. This reaction does not lead to appreciable decrease in crystallinity, which is favorable for subsequent derivation to nanosheets.

Swelling Behaviors in Aqueous TBAOH Solutions. As mentioned earlier, various H-birnessite samples showed different swelling and delamination behaviors in aqueous solutions of quaternary ammonium hydroxides, presumably owing to their different contents of exchangeable protons per MnO_2 unit. The proton content of 0.08 in the present H-birnessite sample was smaller than those of the H-birnessite samples, $H_{0.28}Na_{0.02}MnO_2 \cdot 0.8H_2O$,[11a] $H_{0.22}MnO_2 \cdot 0.62H_2O$,[11c] and $H_{0.13}MnO_2 \cdot 0.7H_2O$.[11b] It should be important to verify the conjecture above and also to provide an alternative approach to the synthesis of MnO_2 nanosheet.

We first examined reaction behaviors of the obtained H-birnessite nanobelt, $H_{0.08}MnO_2 \cdot 0.7H_2O$, in a TBAOH solution of various concentrations.[11b] Birnessite–TBAOH mixtures were equilibrated by shaking for 10 days and then were centrifuged at 6000 rpm to separate into a brown solid and a dark brown supernatant solution. The obtained sediments were subjected to XRD measurements in a wet state,

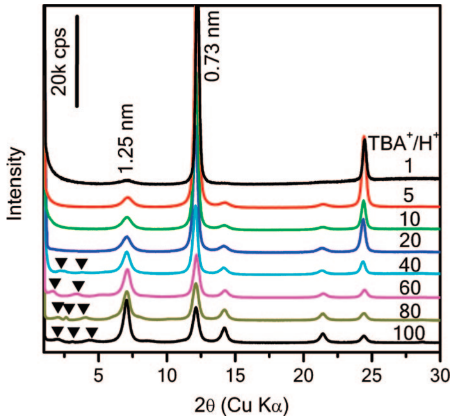

Figure 5. XRD patterns of the aggregates centrifuged from the mixtures of H-birnessite and TBAOH with the TBA$^+$/H$^+$ ratio of 1–100.

and the supernatant solutions were diluted and deposited on a Si wafer chip precoated with PEI for AFM observations. XRD measurements of the sediments detected two noticeable basal diffraction series with a spacing of 0.73 and 1.25 nm throughout the concentration range explored (Figure 5). The latter phase increased in abundance as the ratio of TBA$^+$/H$^+$ increased. The former is due to the pristine H-birnessite, and the latter can be identified as a TBA intercalated phase.[11b] In addition, some rather weak basal reflection series (designated by triangles) were discerned in a low angular range for the samples at high TBA$^+$/H$^+$ ratios (>40). This feature indicates the concurrent occurrence of high degrees of swelling. These reaction behaviors are rather different from our previous results for $H_{0.13}MnO_2\cdot0.7H_2O$. $H_{0.13}MnO_2\cdot0.7H_2O$ was totally converted into the 1.25 nm phase at TBA$^+$/H$^+$ ratio of ≥2. Furthermore, the abundance of highly swollen components was much larger for $H_{0.13}MnO_2\cdot0.7H_2O$ in comparison with the H-birnessite in the present study.

All the supernatant solutions contained exfoliated nanosheets with a lateral size of 10–400 nm (Figure S6).[16] The sediment could be converted into H-birnessite by treatment with HCl solution, and, from its weight, the exfoliation rate for TBA$^+$/H$^+$ ratio of >2 was estimated to be 25–35%.

Swelling Behaviors in Aqueous TMAOH Solutions. The nanosheets obtained by the reaction with the TBAOH solution were not of satisfactory quality in terms of the lateral size, size distribution, and the exfoliation rate. Since the starting H-birnessite crystals were long nanobelts with widths in the micrometer order, delamination into nanosheets with a large size and especially with an inherited beltlike morphology would be the most desirable. Recently, Ooi's group reported a unique delamination procedure, which involves washing the TMA-intercalated birnessite with water.[11a,c] This method can effectively prevent severe fracture of samples because no vigorous shaking is involved. We therefore attempted to take advantage of this method for delamination of the present H-birnessite nanobelts.

As the first step, mixtures of birnessite–TMAOH at various TMA$^+$/H$^+$ ratio were equilibrated for 2 days to examine the swelling behavior. All samples immediately separated into a solid at the bottom of the flask and a clear supernatant solution when shaking was stopped. XRD data for wet aggregates collected by centrifugation from the samples of TMA$^+$/H$^+$ < 30 contained sharp basal reflections (0.73 nm) due to the original H-birnessite, which diminished and disappeared as the TMA$^+$/H$^+$ increased to 30. A broad diffraction envelope in a 2θ range below 10° was merely discerned in the TMA$^+$/H$^+$ range of 30–50. As the TMA$^+$/H$^+$ increased to 50–100, a weak peak developed together with the diffraction envelope. Specifically, the basal spacing of the swollen materials was about 10 and 7 nm for TMA$^+$/H$^+$ = 60 and 80, respectively, if we take this peak as the second-order basal reflection. When TMA$^+$/H$^+$ ≥ 100, the patterns showed well-defined basal reflection series. The basal peaks steadily shifted to a higher angular region and became sharper with increasing TMA$^+$/H$^+$. These results indicate that better crystalline swollen structures developed at higher TMAOH concentrations due to the enhancing interaction between the layers in a shorter separation. The extrapolation of this tendency suggests that the samples in the TMA$^+$/H$^+$ range of 30–50 may have had a very large interlayer distance (>10 nm). The large interlayer separation leads to an extremely weak interaction between the host layers, which may induce some structural disorder to produce the broad profile. The basal spacings decreased from 5 to 1.54 nm as the TMA$^+$/H$^+$ increased from 100 to 500. The basal spacing of 1.54 nm has been attributed to a hydrate structure accommodating one layer of TMA$^+$ ions and bilayer of water molecules in the interlayer gallery.[11a] Further increasing TMA$^+$/H$^+$ up to 1000 did not give a change in the peak position. Apparently, TMAOH showed a much stronger swelling effect than TBAOH. This difference has been interpreted to mean that the intrinsic selectivity coefficient for intercalation tended to increase with a decrease of the size of guest cations.[11a]

The degree of swelling was inversely proportional to the square root of the TMA$^+$ concentrations, as shown in the right panel of Figure 6, indicating the occurrence of osmotic swelling. A similar tendency has been observed for a layered protonic titanate in a TBAOH solution and clay minerals in aqueous media.[11b,17,18] This result is apparently different from the dominant short-range swelling (i.e., the formation of a 1.54 nm swollen phase) for $H_{0.28}Na_{0.02}MnO_2\cdot0.8H_2O$ and $H_{0.22}MnO_2\cdot0.62H_2O$ reported by Ooi's group,[11a,c] verifying our presumption that the quantity of exchangeable protons in the H-birnessite has a significant effect on its swelling behavior.

---

(16) This small lateral size indicates the severe fracture of the pristine nanobelts into small fragments due to the strong mechanical shearing applied in the course of the reaction. The exfolation did not proceed without vigorous shaking.

(17) Sasaki, T.; Watanabe, M. *J. Am. Chem. Soc.* **1998**, *120*, 4682.

(18) (a) MacEwan, D. M. C.; Wilson, M. J. In *Crystal Structures of Clay Minerals and Their X-ray Identification*; Brindley, G. W., Brown, G., Eds.; Mineralogical Society: London, 1980. (b) Schöllhorn, R. *Intercalation Chemistry*; Whittingham, M. S., Jacobson, A. J., Eds.; Academic Press: New York, 1982. (c) Glaeser, R.; Méring, J. *C. R. Held. Séanc. Acad. Sci., Paris* **1968**, *267*, 436–466. (d) Moore, D. M.; Hower, J. *Clays Clay Miner.* **1986**, *34*, 379–384. (e) Watanabe, T.; Sato, T. *Clay Sci.* **1988**, *7*, 129–138. (f) Yamada, H.; Nakazawa, H.; Hashizume, H.; Shimomura, S.; Watanabe, T. *Clays Clay Miner.* **1994**, *42*, 77–80.

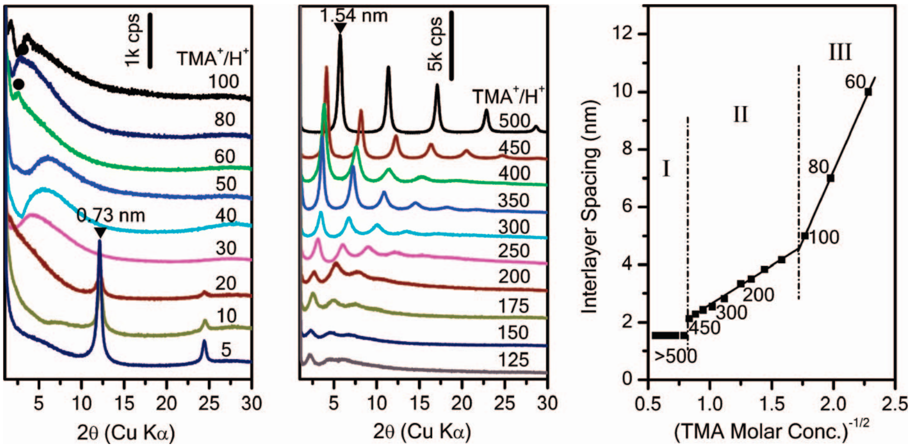

Figure 6. (left two) XRD patterns of colloidal aggregates centrifuged from the $H_{0.08}MnO_2 \cdot 0.7H_2O$–TMAOH mixtures at a molar ratio of TMA^+/H^+ of 5–500. The content of $H_{0.08}MnO_2 \cdot 0.7H_2O$ was 4 g dm^{-3}. The peaks designated by circles could be assigned to the second order of basal reflection series according to the changing tendency with the TMA^+/H^+ ratios. (right) Interlayer spacing as a function of the reciprocal of the square root of TMAOH concentration. Numerals represent the ratios of TMA^+/H^+.

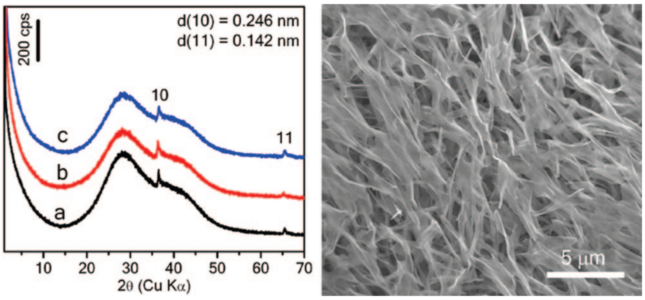

Figure 7. (left) XRD patterns of the water-washed aggregates originated from the mixtures of $TMA^+/H^+ = 30$, 100, and 500 for profile a, b, and c, respectively. (right) Typical SEM image of the water-washed aggregates after drying.

Three linear relationships in the right panel of Figure 6 indicate that the swelling for the current system may be divided into three regions. The data in the superhigh TMA content region, i.e., domain I, represent a stable form of short-range swelling or a threshold of osmotic swelling, while the other domains denote the typical osmotic swelling. The linear relationship of domains II and III showed different slopes at a TMA concentration of ~0.35 M (corresponding to TMA^+/H^+ ~110), indicating some change in swelling, although a quantitative explanation for the change is not available at present.

The colloidal aggregates separated from the H-birnessite–TMAOH mixtures of $TMA^+/H^+ \geq 30$ were treated repeatedly by water washing and centrifuging. A repetition of 5–8 times yielded a pH value of pure water for the supernatant solution, suggesting the complete removal of free TMAOH. All the centrifuged aggregates produced very similar XRD profiles, as depicted by the left panel of Figure 7. These patterns displayed a noticeably broad diffraction halo in a 2θ range of 15°–50° due to X-ray scattering by water. They also contained two weak reflections at 36.5° and 65.5° in 2θ that can be indexed as 10 and 11 for a two-dimensional hexagonal unit cell with $a = 0.284$ nm, indicating that the basic layer architecture remained unchanged. Characteristic basal reflections of the original TMA-intercalated samples were absent. SEM observations (right panel of Figure 7) revealed that these sediments after drying were composed of thin beltlike structures with abundant surface wrinkles. The unchanged beltlike morphology suggests that only a swelling event had taken place. Structure collapses induced by evacuation of interlayer water may be responsible for the formation of wrinkles. Furthermore, when these sediments were treated by an aqueous solution of acids or salts, highly crystalline birnessite nanobelts were restored instantly, as demonstrated by XRD, TEM, and SEM measurements (Figures S7 and S8). The morphological recovery also supports the presumption that the materials obtained by water-washing were not exfoliated but were still in a swollen state possibly with three-dimensional order.

The water-washed samples had a noticeably expanded volume. If we assume that the basal spacing was too large to be detected by the present XRD measurements, it should be as large as several tens of nanometers or more. Even in such a structure, there should be a weak but nonnegligible electrostatic interaction (between interlayer TMA^+ ions and the negatively charged layers) and hydrogen bonding (between the layers and interlayer water molecules) to maintain the swelling. These results are in sharp contrast to reactivity of $H_{0.28}Na_{0.02}MnO_2 \cdot 0.8H_2O$ and $H_{0.22}MnO_2 \cdot 0.62H_2O$, of which the TMA-intercalated phases could undergo delamination into single layers just by washing with water.[11a,c] Absence of exfoliation of the present H-birnessite may be understood by the fact that the amount of intercalating TMA^+, which is determined by the amount of exchangeable protons of the precursor H-birnessite, was too small to produce a sufficiently large hydration repulsive force to overwhelm the attractive forces between the layers.

Exfoliation into MnO_2 Nanosheets. On the basis of the above discussion, the delamination may be promoted by increasing the repulsive force through introducing more hydrophobic quaternary ammonium ions (e.g., TBA^+ or TPA^+) into the interlayer space. Thus the highly swollen materials obtained by water-washing the TMA^+ treated sample were equilibrated with 25 mL of TBAOH aqueous solution of various concentrations. The TBA^+/TMA^+ molar ratio in the mixtures was varied in the range of 0.5–125.[19]

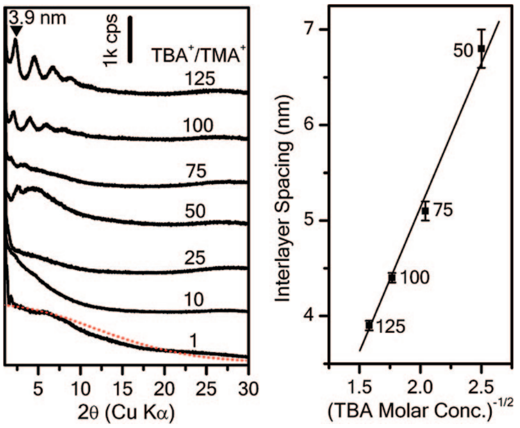

Figure 8. (left) XRD patterns of colloidal aggregates centrifuged from the mixtures of the TMA^+-swollen structure and TBAOH with a TBA^+/TMA^+ of 1–125. A centrifugation speed of 6000 rpm was employed for the samples of $TBA^+/TMA^+ \geq 50$ and 20 000 rpm for others. Note that all samples contained the same amount of TMA^+-swollen structures, which corresponds to 4 g dm^{-3} of the original $H_{0.08}MnO_2 \cdot 0.7H_2O$. The red dotted plot represents the square of calculated structure factor of the exfoliated MnO_2 single layers. (right) Interlayer spacing as a function of the reciprocal of the square root of TBAOH concentration. Numerals represent the ratios of TBA^+/TMA^+.

The resulting mixtures were gently shaken at 80 rpm for 2 days and then centrifuged at 6000 rpm.

The mixtures exhibited various appearances after the centrifugation. The samples with a high TBAOH dose ($TBA^+/TMA^+ \geq 100$) separated into a black-brown aggregate and a transparent red-brown supernatant solution, indicative of nearly total separation of solid material. As the TBA^+/TMA^+ ratio decreased, the amount of the separated solid material declined, and almost no solid was sedimented at TBA^+/TMA^+ of ≤ 10. To recover the dispersed substance from these colloidal suspensions, the samples of $TBA^+/TMA^+ \leq 25$ were centrifuged at 20 000 rpm. All the dispersed material could be recovered as a black-brown pastelike aggregate. XRD measurements on the aggregate in their wet state (left panel of Figure 8) revealed the formation of ordered swollen crystallites at a higher TBAOH dose ($TBA^+/TMA^+ \geq 50$). The linear variation of the interlayer spacings against the reciprocal of the square root of TBAOH molar concentrations (right panel of Figure 8) obviously indicates the osmotic swelling behavior. The ready intercalation of TBA^+ into the material should be noted in comparison with the modest reactivity toward the pristine H-birnessite. This may be ascribed to the highly expanded interlayer space with TMA^+ ions. At low TBAOH concentrations ($TBA^+/TMA^+ \leq 25$), the XRD profiles showed only broad diffraction halo pattern in a low angular region, and the intensity of the halo was enhanced as TBA^+/TMA^+ decreased. The aggregates centrifuged from the mixtures of $TBA^+/TMA^+ = 1$ showed the prominent halo pattern up to $2\theta = 30°$, the profile of which is similar to the square of the calculated structure factor for MnO_2 single layers (the dotted line in the left panel of Figure 8), confirming complete delamination into individual sheets. The sample at this composition ($TBA^+/TMA^+ = 1$) gave a dark-brown colloidal suspension. By highly diluting with water, the thick suspension became semitransparent and light brown (inset of Figure 9), which is characteristic of a colloidal suspension of MnO_2 nanosheets. TPAOH was also found to have a similar action for the exfoliation, although the exfoliation rate was relatively lower than that when using TBAOH. These results demonstrate that the intercalation of more hydrophobic quaternary ammonium ions is indeed able to induce the increase of the repulsive force between the host layers and benefits the exfoliation.

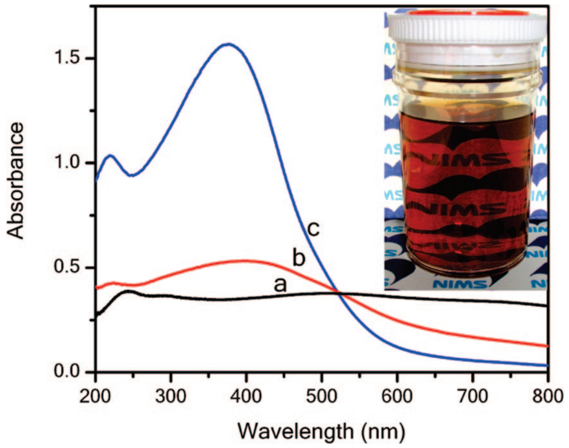

Figure 9. (a) Diffuse reflectance spectrum for the precursor H-birnessite. UV–vis absorption spectra for (b) a suspension of a swollen material obtained by water-washing a TMA^+-swollen phase and (c) a colloidal suspension obtained by shaking a mixture of the swollen material and TBAOH solution at $TBA^+/TMA^+ = 1$. Both suspensions had the same MnO_2 concentration of 0.016 g dm^{-3}. The inset shows a bottle of the diluted colloidal suspension of the exfoliated MnO_2 nanosheets.

The delamination processes from the precursor H-birnessite ($H_{0.08}MnO_2 \cdot 0.7H_2O$) to MnO_2 single layers (nanosheets) could be monitored by UV–vis absorption spectra (Figure 9). The diffuse reflectance spectrum of the precursor H-birnessite (curve a) showed an almost constant and featureless absorption over a wavelength range of 300–800 nm, which is consistent with the previous report.[11b] In contrast, the material obtained by water-washing a TMA^+-swollen phase exhibited a noticeable optical absorption band with a broad peak centered at 380 nm (curve b). When the material was delaminated into a colloidal suspension, the absorption band became much sharper. A large molar extinction coefficient of 8.5×10^3 mol^{-1} dm^3 cm^{-1} was obtained (curve c).

The morphological and structural features of the exfoliated nanosheets were examined by AFM, TEM, and SAED. The AFM image (Figure 10) detected two-dimensional ultrathin sheets with a lateral dimension in the range of 300–1500 nm, although fragments were also observed in small amounts. The height profile revealed that the nanosheets had an average thickness of 0.81 ± 0.02 nm, confirming the unilamellar nature of the exfoliated nanosheets. A typical TEM image (Figure 11a) shows thin sheetlike objects with lateral dimensions similar to those observed in the AFM image. During the TEM observations, some beltlike nanosheets with lengths of several micrometers were occasionally

---

(19) The TMA^+ content in the water-washed sample (i.e., the highly swollen material) should be approximately equal to the proton content of the starting H-birnessite material because repeated water-washing and centrifugation should remove free TMA^+ in the solution. Thus, the TMA^+ content in the mixture of TBAOH and the swollen material was referred to the proton content of the starting H-birnessite.

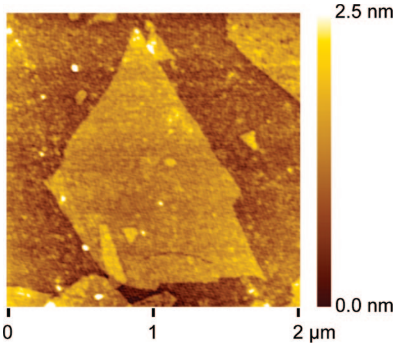

Figure 10. Tapping-mode AFM image of the exfoliated MnO_2 nanosheets deposited on a Si wafer.

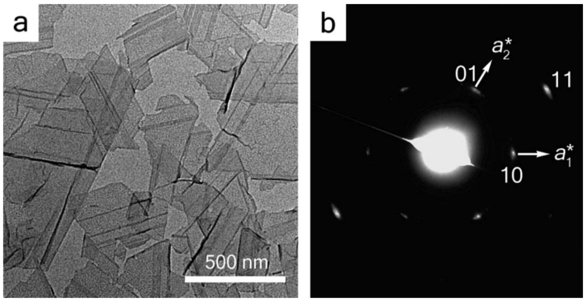

Figure 11. (a) TEM image and (b) SAED pattern of exfoliated MnO_2 nanosheets.

encountered (Figure S9). The faint but homogeneous contrast of the sheets reflected their uniform thickness of <1 nm. Most of the sheets had two parallel straight edges. This particular morphology is likely inherited from the beltlike shape of the parent crystals. The SAED pattern (Figure 11b) of individual nanosheets exhibited diffraction spots in a hexagonal arrangement, verifying the single-crystal quality. The hexagonal lattice constant of a ~0.28 nm was consistent with the two-dimensional structural parameter of the precursory H-birnessite crystal, indicating that the basic architecture was preserved after exfoliation.

Conclusion

Synthesis of high-quality K-birnessite nanobelts and delamination of the protonated form into MnO_2 nanosheets were successfully attained. Highly crystalline and large K-birnessite nanobelts were synthesized by hydrothermally treating a $KMnO_4$–$MnCl_2$ mixture in a concentrated KOH aqueous solution under optimized conditions. The growth of the nanobelts was revealed to follow a dissolution–recrystallization mechanism. Both the KOH concentration and the Mn^{2+}/MnO_4^- molar ratio in the starting reaction mixture were found to have significant effects on the nanobelt growth. The treatment of the K-birnessite nanobelt with the weakly acidic $(NH_4)_2S_2O_8$ aqueous solution at 60 °C produced the protonated form with Z_{Mn} largely increased from 3.67 to 3.92. The treatment with TBAOH aqueous solutions promoted intercalation but delamination only at a limited degree. In contrast, osmotic swelling dominantly occurred upon contact with TMAOH solutions; a series of ordered swollen structures could form with an expanded interlayer spacing in the range of 1.54 nm to tens of nanometers, depending on the TMAOH concentration. Water-washing these TMA^+-intercalated swollen phases led to higher-level swollen structures with a considerable interlayer spacing presumably up to several tens of nanometers. Total exfoliation into single sheets could be achieved by mixing the swollen structures with a TBAOH solution under suitable conditions, yielding nanosheets with a lateral size of micrometer order. By using these large MnO_2 nanosheets as building blocks, a variety of nanostructured systems will be attained via various assembling modes as described previously,[5e,20] resulting in high physicochemical performances.

Acknowledgment. This study was supported by CREST of the Japan Science and Technology Agency (JST).

Supporting Information Available: TG-DTA data for as-prepared K- and H-birnessite samples, XRD pattern and SEM image of the birnessite sample obtained before hydrothermal treatment, SEM images of the samples prepared with various KOH concentrations or Mn^{2+}/MnO_4^- ratios, AFM images of the MnO_2 nanosheets exfoliated by the treatment with TBAOH, XRD patterns and SEM images of various birnessite samples recovered from the highly swollen structures by the treatment with aqueous solutions of acid or salt, and TEM image of the exfoliated beltlike nanosheets. This material is available free of charge via the Internet at http://pubs.acs.org.

CM7019203

---

(20) (a) Wang, L.; Omomo, Y.; Sakai, N.; Fukuda, K.; Nakai, I.; Ebina, Y.; Takada, K.; Watanabe, M.; Sasaki, T. *Chem. Mater.* **2003**, *15*, 2873. (b) Wang, L. Z.; Ebina, Y.; Takada, K.; Sasaki, T. *Chem. Commun.* **2004**, 1074. (c) Wang, L.; Ebina, Y.; Takada, K.; Kurashima, K.; Sasaki, T. *Adv. Mater.* **2004**, *16*, 1412. (d) Wang, L. Z.; Sakai, N.; Ebina, Y.; Takada, K.; Sasaki, T. *Chem. Mater.* **2005**, *17*, 1352.